

Single Laser Pulse Effects on Suspended-Au-Nanoparticle Size Distributions and Morphology

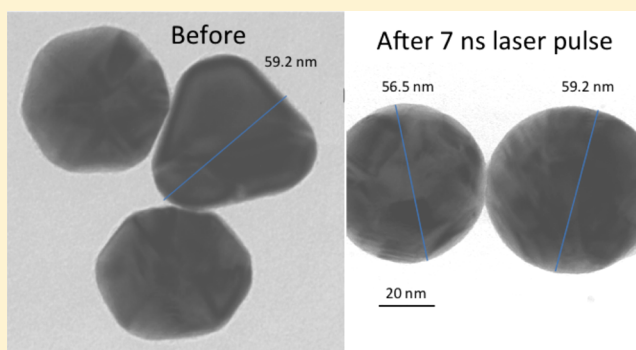
Richard E. Cavicchi,^{*,†} Douglas C. Meier,[†] Cary Presser,[†] Vivek M. Prabhu,[†] and Suvajyoti Guha^{‡,§}

[†]National Institute of Standards and Technology, Gaithersburg, Maryland 20899, United States

[‡]University of Maryland, College Park, Maryland 20742, United States

S Supporting Information

ABSTRACT: Samples of suspended gold nanoparticles in the diameter range 10 to 100 nm were subjected to a single 7 ns pulse from a 532 nm laser to determine the effect of laser power on particle size distribution, mean size, and morphology. The experimental techniques used were dynamic light scattering (DLS), depolarized dynamic light scattering (DDLS), electrospray-differential mobility analysis (ES-DMA), ultraviolet–visible absorption spectroscopy, and transmission electron microscopy (TEM). For 60 nm particles, a laser pulse of fluence 10 mJ/cm² was sufficient to produce observable changes. In the range 10–72 mJ/cm², DLS indicated little change in mean particle size but a more than three-fold reduction in the polydispersity index (significantly tightened distribution) and a decrease in scattering intensity. TEM showed that the particles became highly spherical and that there was a growing population of particles <10 nm in size that could not be detected by DLS and ES-DMA. Fused dimers were also observed, which suggest that heated particles can interact prior to cooling. DDLS showed a decrease in scattering due to shape anisotropy with a 20 mJ/cm² pulse and a decrease in the diffusion time constant. At higher power, the mean particle size decreased until all particles were <10 nm in size. The threshold for observable changes decreased with increasing particle size in the range 10 to 60 nm but increased for 100 nm particles. These results will be useful for potential therapeutic applications for pulse-heated nanoparticles and demonstrate the use of a simple laser treatment for modifying and improving nanoparticle properties.



INTRODUCTION

A promising avenue of nanomedicine research centers on the laser heating of metal nanoparticles (NPs) that have been delivered to a targeted part of the body for thermal therapies^{1–10} or to trigger release of an encapsulated drug.^{11–14} Gold NPs have received significant attention because of the advantages of biocompatibility,¹⁵ ability to be functionalized, and a surface plasmon resonance (SPR) that enhances the optical absorption of the NP relative to its surroundings. A variety of particle shapes have been investigated for laser heating applications, including metal nanospheres,¹⁶ nanoshells,^{1,7,17–24} nanorods (NRs),^{9,10,25–36} nanocages,³⁷ and nanopyramids.³⁸ Nonspherical shapes have been used with the purpose of tuning the peak wavelength of the SPR.

Energy absorbed by the NP is conveyed to the environment of the NP through thermal diffusion. Continuous-wave (CW) laser exposure has been used to achieve temperature increases suitable for therapeutic effects.^{8,19,24,34,39} Laser CW heating does not result in a significant temperature gradient between particles and their surrounding environment; however, essentially all of the thermal energy absorbed by a particle is used to increase the temperature of the particle's environment.^{40–43} It has been shown that the energy relaxation in a Au NP takes place on a

picosecond time scale.^{44–46} Thus, the use of pulsed laser radiation can produce significant heating on the submicrometer scale, both because much higher power levels can be used and because the thermal diffusion length over the duration of the pulse will be short. Nanosecond pulsed lasers have been used to kill cancer cells with a mechanism that can involve the generation of high-energy fragments⁴ or the formation of an explosive bubble around the NP.^{6,16,47–52} Delivering 30 nm NPs to cancer cells, Huang et al.⁵² found that a 7 ns pulse from a 532 nm laser resulted in comparable cell death rate to a CW laser but with a total energy deposition reduced by more than a factor of 10⁵.

The fundamental nature of the processes that occur on the nano- and microscale during the pulsed heating of NPs is of continuing intense interest. Takami et al.^{53,54} treated silver and gold NPs in aqueous solution with a repeated nanosecond pulsed laser and observed, by transmission electron microscopy (TEM) analysis, a reduction in the particle size. Using silver 40 to 60 nm NPs under repeated 20 ps pulses at 7.5 mJ/cm², Kamat et al.⁵⁵ observed photofragmentation into 5 to 20 nm. Pump–probe experiments that showed a bleaching effect on the SPR suggest a

Received: April 26, 2013

Published: April 30, 2013

mechanism that includes electron ejection from the NP. Link et al.^{44,56} investigated the melting, fragmentation, and reshaping of Au NRs with femtosecond and nanosecond laser pulses. They reported that with femtosecond pulses only melting of the NRs occurs, but for nanosecond pulses fragmentation occurs, which they explain as being due to the absorption of photons by the hot lattice. Giammanco et al.⁵⁷ proposed a model for laser ablation of NPs that considered the processes of ionization and evaporation for reducing particle size. For their 3.5 nm particles and 20 ps pulse conditions, a dominant ionization process best fit the data. Matsuo et al. and Muto et al.^{58,59} applied single 532 nm laser pulses to 80 μm diameter droplets containing 11 nm NPs and observed fragmentation into smaller particles that then aggregated. Yamada⁶⁰ obtained transient absorption spectra from 8 nm Au NPs subjected to 10 ns 355 nm laser pulses and assigned the particle fragmentation to a Coulombic explosion process. Hleb and Lapotko⁶¹ have reported a detailed comparison of the photothermal properties for nanosecond pulses of three particle shapes: nanosphere, NR, and nanoshell. Among the interesting findings in this article is the observation that the plasmon properties of NRs and nanoshells are markedly different at high fluence (near the laser-damage threshold) compared with the properties at low fluence, so that even though the engineered particles have an absorption maximum in the IR the threshold for damage is lower in the visible. Nanobubble generation around the NPs was also characterized in that work by both stroboscopic photography and defocusing of a 633 nm probe beam. From the data presented in the article, one can conclude that nanobubble generation is at intensities at or above the threshold for particle damage. Lapotko et al.⁶² have also demonstrated that nanobubbles may be used for optical detection.

From the works cited above, it is clear that laser-induced damage is a critical factor in the application of pulsed lasers for the heating of NPs. The absorption of energy depends on the size of the particle. Pitsillides et al.¹⁶ observed that when ablated by 20 ns, 532 nm laser pulses with an amplitude of 0.5 J/cm², 30 nm particles caused cell death while 20 nm particles only altered the permeability of a cell membrane.

In this study, we report the spectroscopic and structural effects of a 7 ns, 532 nm frequency-doubled pulsed Nd:YAG laser on particles with five different sizes, 10, 20, 30, 60, and 100 nm, as a function of laser fluence ranging from 4 to 390 mJ/cm². This size range is important for nanomedicine applications because NPs smaller than 10 nm are rapidly eliminated through the kidney while particles in the range 10 to 100 nm travel throughout the bloodstream and can be transported into the tumor tissue.⁶³ We focus on the effects of a single laser pulse rather than a series of pulses delivered over a specific time interval. If damage is occurring to the particle, it is most likely that the most significant therapeutic effect will occur during the first pulse. To probe for changes in the particles in their liquid environment, we make use of dynamic light scattering (DLS), which provides information on the size and concentration (based on overall scattering intensity), electrospray-differential mobility analysis (ES-DMA), which provides particle size distributions, and ultraviolet–visible absorption spectroscopy (UV–vis), which provides evidence of changes in the particle's plasmon resonance. In addition, we have used TEM to characterize changes in particle morphologies.

■ EXPERIMENT

Commercially available monodisperse, citrate-stabilized, Au colloids (with nominal diameter, concentrations of 10 nm, 5.7

$\times 10^{12}$ particles/mL; 20 nm, 7.0×10^{11} particles/mL; 30 nm, 2.0×10^{11} particles/mL; 60 nm, 2.6×10^{10} particles/mL; 100 nm, 5.6×10^9 particles/mL; from Ted Pella⁶⁴) were used in this investigation. Laser exposures were performed with a Q-switched Nd:YAG laser, Surelite II, with the 1064 nm line frequency-doubled to produce a 532 nm beam. The full width at half-maximum time for the laser pulse was measured to be 7.46 ns. The beam intensity profile was measured by moving a 0.5 mm pinhole across the diameter of the ~ 7 mm beam spot. It was found that the power decreased from a maximum at the center to 80% of the maximum at a radius of 2 mm. The samples were typically 300 mL in volume and were divided into equal 100 μL aliquots for laser exposure. This procedure assured that the Beer's law attenuation caused insignificant variation in the exposure of particles in the 3 mm depth of the liquid container. The liquid container was a 0.65 mL microcentrifuge tube with an outer diameter of 4 mm for a 100 μL aliquot. The beam was directed downward to the open top of the container. The beam fluence applied to the sample was varied from 0 (untreated) to 390 mJ/cm² through the use of neutral density filters. A fresh sample was used before each exposure to the laser.

Backscatter DLS measurements were performed using a Malvern Zetasizer-Nano ZS. The laser wavelength was 633 nm (He–Ne). The scattering angle was 173°. Measurements were made at 20 °C. Typically 12 scans were averaged for each measurement and 5 to 8 measurements were performed for each sample after the laser exposure. The autocorrelation function was analyzed by the cumulants method in the instrument software according to ISO13321 Part 8.⁶⁵ The analysis yields a mean particle size expressed as a diameter and a polydispersity index (PDI). The PDI is a measure of the width of the size distribution. If the size distribution is a single Gaussian, then the standard deviation σ of the distribution will be $\sigma = (\text{PDI})^{1/2}x$, where x is the mean size. This analysis is considered to be valid for monomodal systems. For bimodal distributions (which occurred only for the 10 nm NPs and as a result of the highest laser exposure to the 100 nm NPs), the mean particle size was analyzed with a non-negative least-squares (NNLS) fit.⁶⁶ The average scattered intensity signal was also collected for each scan. The instrument reports scattered intensity as kilocounts per second, which is regarded as an arbitrary intensity unit. With each sample (and therefore each fluence value) the scattering intensity of the sample prior to the laser pulse treatment was collected and used to normalize the intensity data after the laser pulse. Error bars represent the standard deviation in the scatter of the measurements taken on each sample.

Additional experiments were carried out with a second DLS apparatus for the purposes of corroborating the results at a different scattering angle and to make use of the capability of the second apparatus for performing depolarized dynamic light scattering (DDLS), which can provide information about shape anisotropy. This apparatus used a diode-pumped solid state laser at 532 nm wavelength to produce a linearly polarized laser beam of 0.7 mm diameter. The beam was focused with an f -180 mm achromatic doublet lens in the center of a square quartz sample cell. The spectroscopic cell had internal dimensions of 10 mm \times 2 mm that required ~ 0.125 mL of solution. Light, quasi-elastically scattered at 90°, passed through a rotatable polarizer (analyzer) and was collected by an f -8 mm aspherical lens and coupled to a single-mode fiber with 4.3 μm core size. The bifurcated fiber was connected to a two-avalanche photodiode photon counter and counts were cross-correlated by a Brookhaven Instruments BI9000AT digital correlation board.

The incident laser power of 35 mW was reduced by a set of neutral density filters to keep the photon count below 1 MHz in the detector's linear range. With a vertically aligned analyzer (VV), DLS data were obtained with a 2 min collection time, while DDLS with crossed polarizers (HV) required a 10 min collection time. The DLS data were fit with quadratic cumulant and CONTIN methods provided by Brookhaven Instruments software to determine the hydrodynamic diameter and polydispersity. DDLS were fit by the quadratic cumulant method and analyzed to estimate the rotational diffusion coefficient (Θ_r) using the relationship, $\Gamma_{HV} = D_t q^2 + 6\Theta_r$, where Γ_{HV} is the measured decay rate, q is the scattering vector, and D_t is the translational diffusion coefficient determined by DLS.⁶⁷ The Θ_r provides sensitivity to changes in NP shape anisotropy before and after laser-pulsed treated gold NPs.

The optical absorption spectra were obtained using a Perkin-Elmer Lambda Bio-20 UV-vis spectrometer. The samples were measured using a 1 cm path length quartz cuvette. The absorption spectrum was measured from 900 to 400 nm at a scan rate of 240 nm/min and a step size of 1 nm.

Electrospray differential mobility analysis (ES-DMA) was employed as an orthogonal characterization technique for comparison of the effects of lower laser power on the particle size. The ES-DMA system has been previously described.⁶⁸ It consisted of an electrospray aerosol generator (model 3480, TSI), a differential mobility analyzer column (model 3080n, TSI), and a condensation particle counter (CPC, model 3025, TSI). Flow handling to the DMA column and the interface of the instruments employed a home-built design. A 40 μm capillary was used inside the ES, and the NPs were driven toward the DMA by air at a flow rate of ~ 1.2 L/min. A sheath flow rate of 10 L/min was used inside the DMA, and the CPC was used at high flow mode. Under the operating conditions the maximum variability in size and concentration is ~ 0.3 nm and $\sim 15\%$, respectively.⁶⁹ Aliquots of 1000 mL that contained gold NPs of nominally 30 and 60 nm diameter that were either laser-treated (at 72 and 31 mJ/cm² respectively) or left untreated were concentrated in a centrifuge⁷⁰ for 5 to 10 min at a relative centrifugal force of 16110 g. About 800 mL of the supernatant was removed, increasing the concentration of the analyzed samples by a factor of 5. Two replicate samples were used for each set of conditions. The standard deviation (as a percentage) in concentration was 3.7 and 8.3% for the 60 and 30 nm particles respectively. The sources of variation are in order of importance: (a) variation in the ES cone, (b) counting statistics in the CPC, and (c) variation from fluctuations of sheath and aerosol flow.

TEM bright-field images were collected using a Philips/FEI CM300FEG⁶⁴ operating in the high-resolution (HR) bright-field TEM mode at 300 kV. Specimens initially were prepared by dropping 20 μL of the laser-treated Au NP suspensions onto SiN TEM windows; however, because NP suspensions frequently agglomerated upon drying, obscuring much of the information that might otherwise be obtained from the TEM images, a drop-on-rinse-off method was used. Treated suspensions were dropped onto chemically functionalized grid windows, allowed to stand for 1 min, then rinsed off with deionized water. This method resulted in specimens that were found to have only minor agglomeration of NPs and little residual salt.

RESULTS

Figure 1 presents the DLS results for averaged scattered intensity and particle mean diameter as a function of the exposure of a fresh sample to a single pulse of a 532 nm laser.

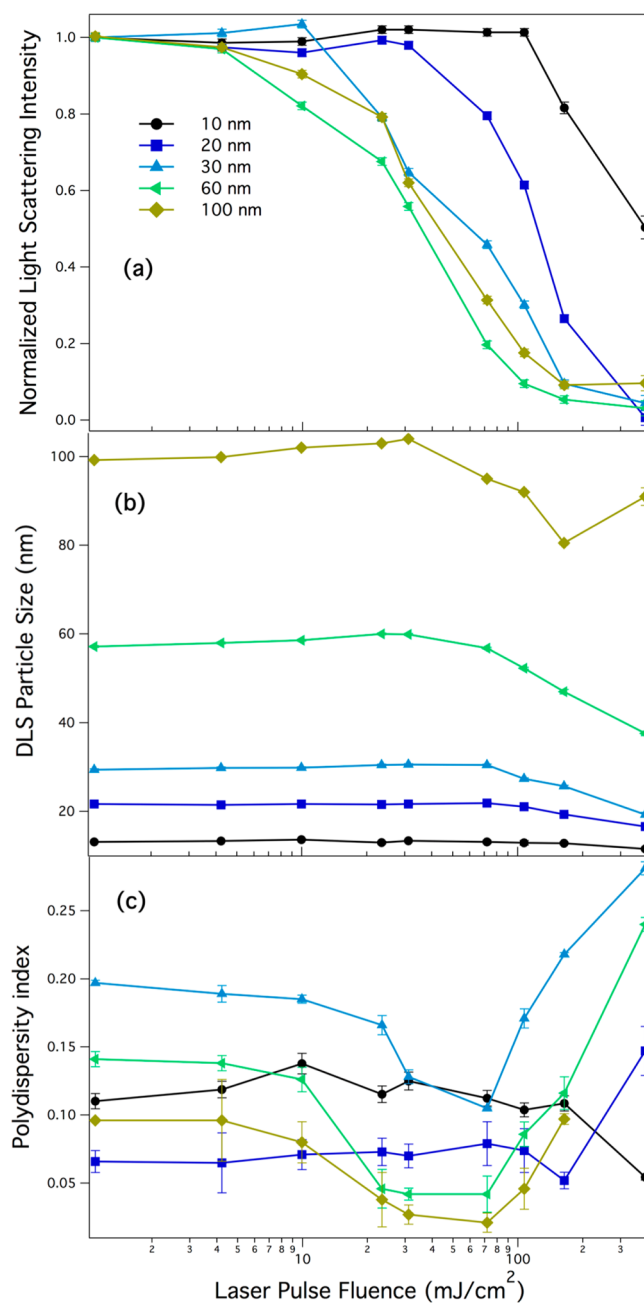


Figure 1. (a) Normalized light scattering intensity at a wavelength of 633 nm, (b) DLS mean particle size (nm), and (c) DLS polydispersity index as a function of the fluence of a single pulse of 532 nm laser irradiation. The data appearing below a fluence of 2 mJ/cm² are the results from untreated samples, included for comparison. Each data point is a separate sample exposed to only one laser pulse. Average starting particle size is as indicated in the legend. For most points in panels a and b error bars are smaller than the data point size. The PDI for 390 mJ/cm² for 100 nm particles was 0.52, outside the plotted range in panel c.

fluence is increased, the trace for each starting size of NP shows a drop of scattered intensity (Figure 1a). The larger initial size NPs exhibit this drop beginning at lower fluence and over a wider range of fluence than the smaller NPs. The observations were not monotonic with size: for example, the 60 nm NPs showed the laser-induced changes at a lower fluence than for the 100 nm NPs. The 20 nm NPs required a much higher fluence of laser pulse to yield a change in scattered intensity, but the drop in

signal occurred more rapidly with laser pulse fluence. This trend continued with the 10 nm NPs, for which the maximum fluence for our experimental arrangement only reduced the scattering intensity by one-half.

As for the effect of the laser pulse on particle size (Figure 1b), we do observe, in most cases, a regime of reduced particle size as a result of the laser exposure. Surprising, however, is that for each size of particle, the reduction in size happens at higher fluence than for the drop in scattered intensity (Figure 1a). For 100 nm, 60 nm, and slightly for 30 nm particles, there is a small increase in DLS particle size before the drop in size at higher pulse fluence. It is interesting, for example, to compare for the 60 nm particle the scattered intensity and DLS particle mean size at 31 mJ/cm². The scattered intensity was reduced by ~50% from the untreated sample, a substantial indicator of the laser's effect on the sample, while the mean particle size increased by 2.7 nm. Because the scattered intensity goes as the sixth power of particle diameter,⁷¹ the expectation would have been that if the intensity decreases as a result of a laser pulse exposure, the particle size would also decrease rather than increase.

Figure 1c shows the dependence of the PDI on laser pulse fluence. For mean diameters of 10 and 20 nm, there is no significant change in the PDI with increasing pulse intensity (up to 100 mJ/cm²). For the 30, 60, and 100 nm NPs, the PDI shows a decrease at lower exposure fluence, followed by an increase for pulse intensities >70 mJ/cm². For these particle sizes, there is a regime between 10 and 70 mJ/cm² where the laser treatment narrows the DLS size distribution significantly, with the PDI decreasing by more than a factor of 3. This effect is evident in the DLS intensity distribution for the 100 nm NPs shown in Figure 2.

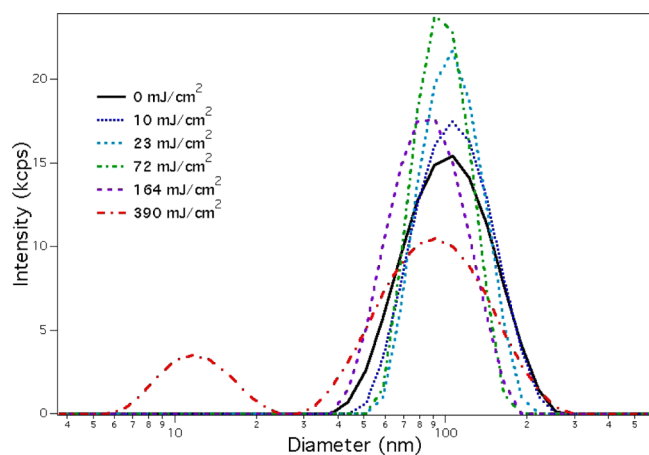


Figure 2. DLS distribution of particle sizes with initial mean diameter of 100 nm for varying energy of exposure to a single pulse of 532 nm laser irradiation. Intensity units are kilocounts per second (kcps) measured by the detector.

The distribution is calculated from the correlogram using the NNLS algorithm that is part of the software for our instrument. Between 10 and 72 mJ/cm² there is a substantial narrowing of the distribution. Between 72 and 390 mJ/cm² the distributions become wider, and at 390 mJ/cm² a second peak at 12 nm appears.

The second DLS/DDLS apparatus was used to compare before and after laser-pulse exposure for 60 nm NPs for a laser pulse fluence of 20 mJ/cm². Results are summarized in table form in the Supporting Information. The DLS-VV results showed a negligible shift in the hydrodynamic diameter from 55.6 ± 0.62

to 56.3 ± 0.97 nm that was within the uncertainty of the measurement but a decrease in polydispersity from 0.155 ± 0.006 to 0.075 ± 0.036. These measurements were in agreement with the trends from DLS measurements performed on the backscattering DLS setup. The conclusions were also verified by a CONTIN analysis that fits the entire autocorrelation function and yielded a shift in the hydrodynamic diameter of 55.2 ± 1.4 to 55.0 ± 1.4 nm with relative variance decreasing from 0.019 ± 0.009 to 0.002 ± 0.002 after the laser pulse. The DDLS measurement tested sensitivity to the NP anisotropy via the rotational diffusion coefficient. For both 60 nm NP samples, there was a measurable depolarized scattering signal, indicating shape anisotropy. The unexposed gold had an average depolarized scattering count rate of 7.4 kHz with a rotational diffusion coefficient measured to be 4471 ± 217 s⁻¹. After laser pulse exposure, the solution decreased in the depolarized scattering count rate to 2.2 kHz, with a rotational diffusion coefficient of 1961 ± 151 s⁻¹.

UV-vis spectra of particles with initial mean diameter of 60 nm for varying fluence of the laser heating pulse are shown in Figure 3. The absorption maximum shifts to shorter wavelength

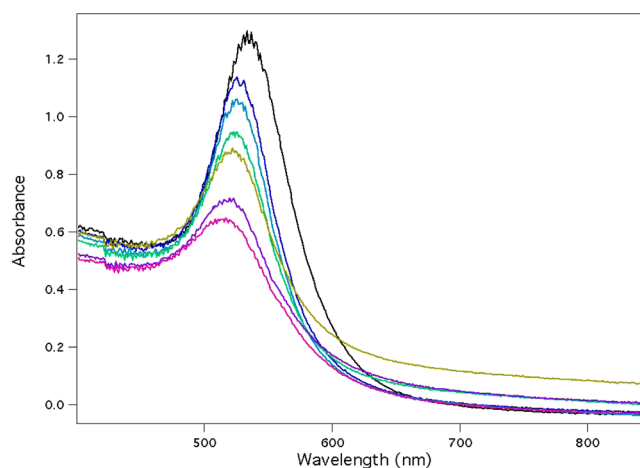


Figure 3. UV-vis spectra of particles with initial mean diameter of 60 nm for varying fluence of exposure to a single pulse of 532 nm laser irradiation. The amplitude of the peak corresponds inversely to the exposure fluence: the largest peak is unexposed, the next largest is 23 mJ/cm², and in order of decreasing peak height, 31, 72, 107, 164, and 390 mJ/cm².

and is of reduced amplitude as the laser pulse fluence is increased. Figure 4 shows a summary of the results for different initial NP size. The behavior is similar for all particles sizes; with the principle difference being the laser power required to produce changes increases with decreasing NP size.

It is important to note that the pulsed laser wavelength differs from the absorption maximum for each NP size. Figure 5 shows the absorbance at 532 nm normalized to the absorbance maximum. These data suggest that the effect of the pulsed laser being detuned from optimal is minimal for NPs with diameters ranging from 10 to 60 nm and is a small effect compared with the range of pulse energies applied for the 100 nm NPs.

Figure 6 shows the results of a DMA comparison between untreated 60 and 30 nm diameter samples exposed to a laser pulse fluence of 31 and 72 mJ/cm², respectively. These cases were selected because the Figure 1 data show little effect of the laser pulse on particle size but substantial effects on scattering

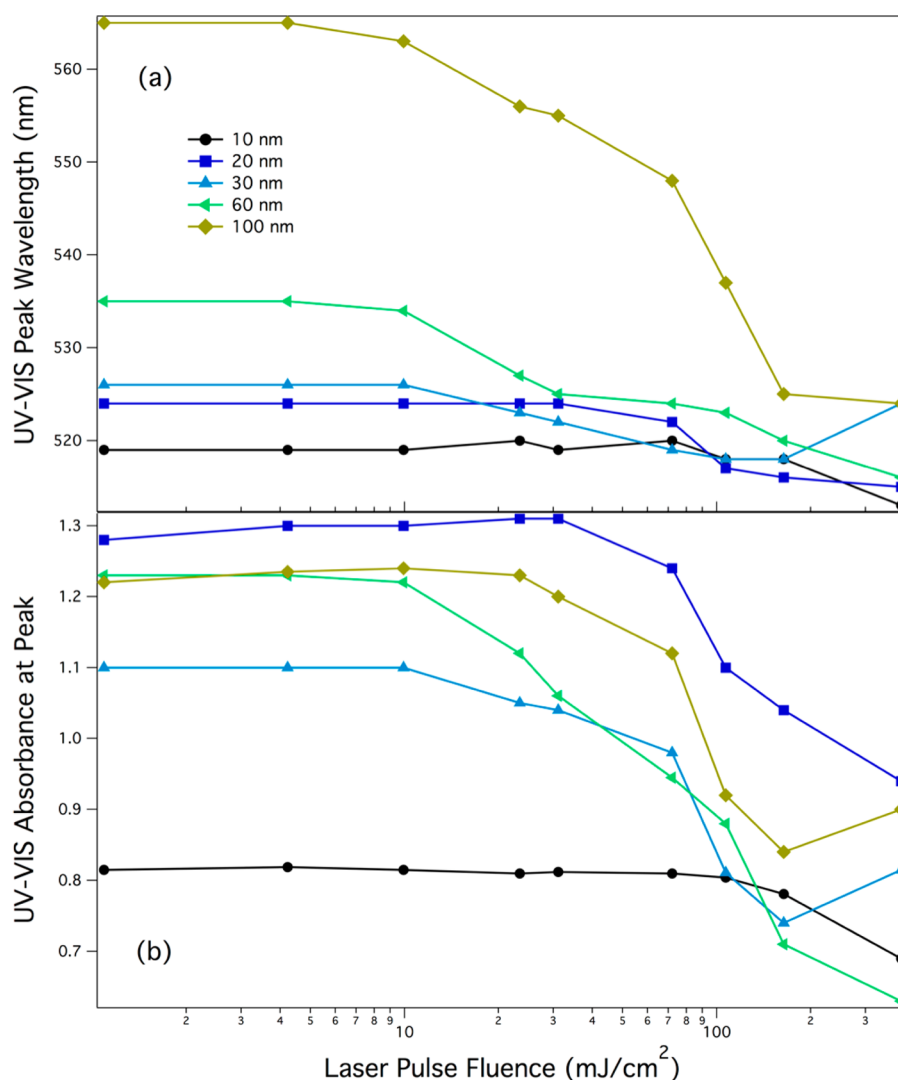


Figure 4. UV-vis results for particles of different initial diameter: (a) Peak wavelength and (b) absorbance at the peak wavelength versus laser pulse intensity. The data appearing below a fluence of 2 mJ/cm² are the results from untreated samples, included for comparison.

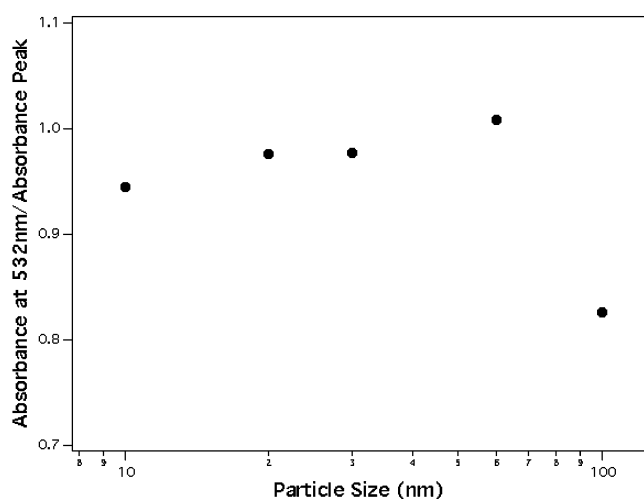


Figure 5. Absorbance at 532 nm, the wavelength of the pulsed laser as a function of particle size.

intensity and polydispersity. In each graph there is a peak at a mobility diameter of 20 nm. In ES-DMA there is typically a “salt

peak” that arises from the residual salt, left when an electro sprayed droplet that does not contain an NP dries. Note that for the 60 nm particles (Figure 6a) the ratio of the salt peak to the Au NP peak is much greater than that for the 30 nm particles. This is because the concentration of particles in the 30 nm samples is nearly ten times higher than that of the 60 nm suspensions. The nominal 60 nm particles decrease in size from 64 to 63 nm as a result of the single laser pulse. The effect of the salt crust layer on these particles is only ~ 0.1 nm, so the reported size represents the estimated size of the Au material.⁶⁸ The nominal 30 nm particles showed essentially no change in size, with measured sizes of 33.1 and 33.2 nm before and after laser treatment. For these particles, the salt layer represents 0.8 nm of the measured particle diameter.

Figure 7 shows TEM images of 60 nm NPs unexposed and exposed to laser pulses ranging from 10 to 72 mJ/cm². The Au NPs as received have a narrow size distribution but exhibit a variety of shapes, including hexagonal, triangular, and circular, as can be seen in Figures 7a,b. While some structure is discernible, the atomic rows indicative of single-crystalline structures cannot be found in these images, indicating that the particles are likely polycrystalline. At low fluence, 10 mJ/cm², as shown in Figures 7c,d, conformational changes are readily observable, in that most

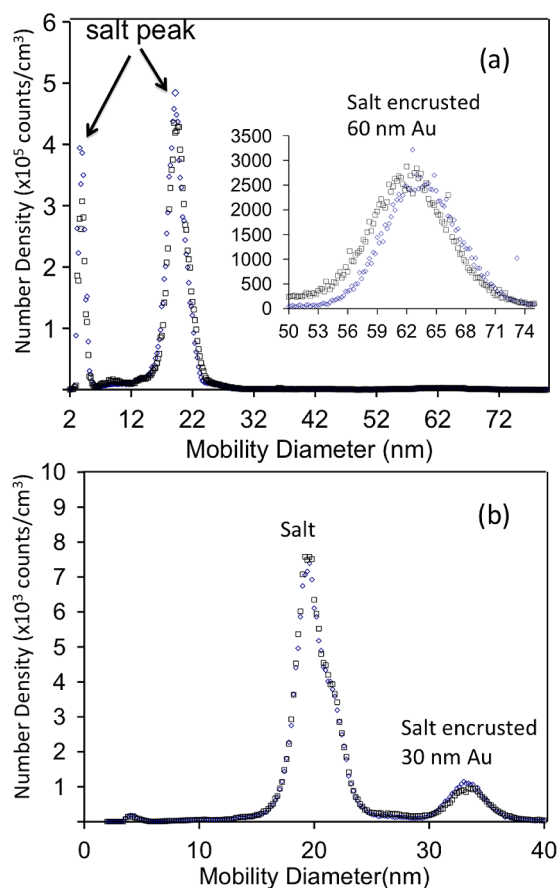


Figure 6. DMA results. (a) Size distribution of untreated 60 nm Au (square) and laser-treated ($31 \text{ mJ}/\text{cm}^2$) 60 nm Au (diamond). The inset shows a zoom of the 60 nm region. (b) Size distribution of untreated 30 nm Au (square) and laser-treated ($72 \text{ mJ}/\text{cm}^2$) (diamond).

larger particles have formed spheres featuring readily distinguishable parallel atomic rows that suggest a greater degree of crystallinity, while other smaller irregularly shaped particles up to 20 nm in diameter now appear in the images. The laser exposure at $10 \text{ mJ}/\text{cm}^2$ also resulted in the formation of some fused dimer species, as shown in Figure 7d, which were not present in the untreated samples. Increasing the pulse power to $23 \text{ mJ}/\text{cm}^2$, as in Figure 7e,f, generates similar particles to those formed by the $10 \text{ mJ}/\text{cm}^2$ pulse. At $31 \text{ mJ}/\text{cm}^2$, Figure 7g,h also shows spherical particles with reduced size and an increase in the smaller irregularly shaped particles. At $72 \text{ mJ}/\text{cm}^2$, the smaller particles dominate (Figure 7i,j), with most particles exhibiting facets and sharp edges over their entire surface.

DISCUSSION

The different characterization tools provide complementary information about the changes that occur to suspended Au NPs with a single laser pulse. DLS provides a rapid characterization of changes in the scattering intensity and changes to the distribution of hydrodynamic size of the NPs. The scattered intensity data showed a strong dependence of the threshold fluence for observable change with particle diameter to smaller values for mean sizes 10 to 60 nm. This is consistent with the reduction in absorption cross section with NP size. By contrast, the 60 nm NP threshold for observable change was lower than that for the 100 nm NPs (see Figure 1a). This trend was also observed in the UV–vis results, where the threshold for change in the peak

amplitude also shows the 60 nm NPs more easily damaged than the 100 nm NPs (see Figure 4b). This suggests that the laser's capability to damage a NP does not depend solely on the absorption behavior that is measured by low-intensity techniques such as UV–vis spectroscopy. In a similar vein, Hleb and Lapotko noted that NRs with an absorption cross section maximum near 750 nm were surprisingly more easily damaged by 532 nm laser pulses than with 750 nm laser pulses.⁶¹ It should be noted that the threshold intensities observed for 100 nm Au NPs were still well below the ablation threshold of bulk Au, reported by Torrisi et al., to be $10 \text{ J}/\text{cm}^2$.⁷²

The decrease in scattered intensity with increasing laser pulse fluence in Figure 1a could be due to one of two factors: (1) a reduction in the number of scattering NPs (possibly caused by some fraction of the NPs being shattered by the laser pulse) or (2) efficiency of scattering by each NP (possibly caused by a reduction in size or change in shape). For the moderate laser fluence exposures of $31 \text{ mJ}/\text{cm}^2$ for the 60 nm and $72 \text{ mJ}/\text{cm}^2$ for the 30 nm NPs, DMA results showed that the number of NPs was relatively unchanged by the pulse, whereas DLS results in Figure 1a showed a decrease in scattering intensity, and UV–vis spectroscopy in Figure 4b showed a decrease in absorption. Thus, the evidence points toward a laser-induced change in the efficiency of scattering of each NP in the distribution for these fluence pulses.

The DLS results for mean size were surprising because while change to the NPs was evident in the scattering intensity data, the size data for low to moderate laser pulse fluence showed little change in size. By contrast, in this fluence range, the UV–vis spectroscopy data showed the absorption maximum to be shifting to smaller wavelength. The location of the absorption maximum in UV–vis spectroscopy has been shown to decrease with decreasing particle size.⁷³ Thus the UV–vis results seemed to suggest that the particles were decreasing in size.

TEM images helped to clarify the seemingly conflicting DLS and UV–vis data. At moderate pulse fluence, particles changed into spherical shapes with larger crystalline domains without changing considerably in size, although some shrinkage was observed directly in the images. Because the normalized DLS scattering intensity began to fall at low exposures while DLS particle size remained roughly constant, it can be inferred that the back scattering intensity decreased as particles became more spherical. Calculations by Lee et al.²⁵ have shown that gold NRs have higher scattering efficiencies than equivalent volume gold nanospheres of diameter 80 nm. The presence in TEM images of laser-treated samples of particles $<10 \text{ nm}$ in size indicates that some reduction in particle volume is taking place in addition to the reshaping. Because the scattered intensity scales as the sixth power of the radius, for a 60 nm diameter particle, a 5 nm change in diameter would result in a 37% drop in scattered intensity. The dramatic reduction in polydispersity seen in the DLS results, for both backscattering and 90° measurements, can also be explained by the convergence of differently shaped particles, including hexagonal and triangular prisms, to spheres. Because the nonspherical particles will have different diffusion coefficients along their different axes, this will result in a spread in the apparent size distribution compared with the spherical particles that are formed as a result of the moderate laser pulse.

The DDLS results confirmed the presence of shape anisotropy in the untreated samples. After the $20 \text{ mJ}/\text{cm}^2$ exposure, there was a decrease in the depolarized scattering intensity and a decrease in the measured diffusion constant. This is consistent with a smaller population of anisotropic particles but with a larger

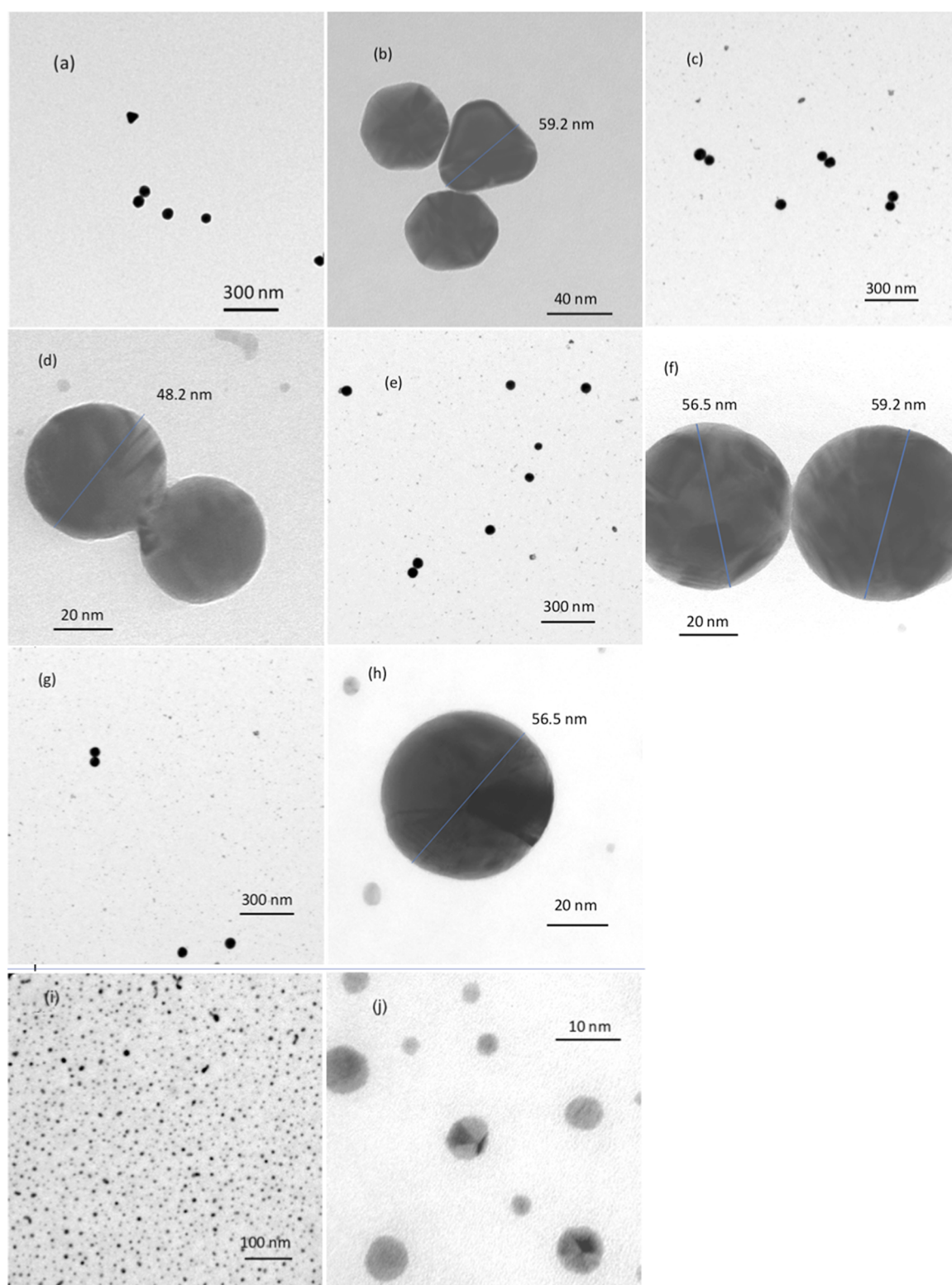


Figure 7. TEM images of the 60 nm diameter NPs (a,b) before laser exposure and exposed to a single pulse of 532 nm laser irradiation at: (c,d) 10 mJ/cm²; (e,f) 23 mJ/cm²; (g,h) 31 mJ/cm²; and (i,j), 72 mJ/cm².

anisotropy among the contributing particles. This may be verified by the TEM evidence that shows not only the change in particle shape but also an increase in the concentration of fused gold nanocrystal dimers that appear only after laser-pulse exposure. We hypothesize that DDLS is very sensitive to the increased formation of these anisotropic NPs in addition to the general

decrease in anisotropy of the individually dispersed NPs of near-spherical shape. To estimate the change in anisotropic shape predicted by the DDLS measurements the data were compared with the rotational diffusion coefficient calculated by Perrin^{67,74} for an ellipsoid of revolution of semi-axes a and b . The procedure is described in the Supporting Information. The results suggest

an increase in axial ratio from 1.3 to 1.8 after exposure with the formation of more prolate-shaped anisotropic particles that are consistent with fused gold particles.

The considerably smaller particles formed during ablation or obliteration do not figure into the scattering experiment results; indeed, only at a laser fluence of 390 mJ/cm² does the laser pulse generate enough small particle debris for it to be detectable. This is due to the strong sixth-power dependence of light scattering on particle diameter. The shift in the UV absorbance to smaller wavelength with pulse fluence can be attributed to a dependence of absorbance on particle shape.⁷⁵ For example, NRs show an increase in absorption peak energy with decreasing aspect ratio.⁷⁶ At higher pulse fluence, the particle size decreased, which also resulted in a shift to higher energy for UV–vis absorbance.

CONCLUSIONS

The effect of single 7 ns laser pulses of varying fluence applied to gold NPs was characterized for particles from 10 to 100 nm by a set of NP characterization tools. As particle diameter increased from 10 to 60 nm, the threshold fluence for causing changes in NP properties decreased, while at 100 nm, the threshold for observed damage appeared to increase. At low fluence, the NPs were reshaped into substantially more round spheres, while at the same time, fragments of <10 nm were generated. These fragments were not detected by DLS due to the strong dependence of scattering intensity on size or by DMA, where the fragments are obscured by the signal from condensed salt. For low laser fluence, the PDI reported by DLS, was reduced by as much as a factor of three, indicating a much narrower hydrodynamic size distribution. Also, fused dimer particles were evident, which suggests that particles heated by a pulse can travel to interact with other particles prior to cooling below the melting temperature. These dimers may be responsible for the decreased diffusion constant measured by DDLS. At higher fluence, >100 mJ/cm², there was substantial fragmenting of all particles. Because of the initial changes observed in particles as a result of a single pulse, including the generation of fragments, it is likely that the use of multiple pulses has limited additional therapeutic benefit compared with a single pulse. The data suggest that with filtering of debris particles <10 nm or by further optimization of the pulse power and duration it should be possible to produce highly spherical NPs in the diameter range 30–100 nm with a low PDI.

ASSOCIATED CONTENT

Supporting Information

DLS and DDLS results from the 90° light scattering instrument. Also presented is a calculation for the rotational diffusion coefficient of an ellipsoid as a function of the axial ratio. This calculation is compared with the experimental results from the DDLS measurement. This material is available free of charge via the Internet at <http://pubs.acs.org>.

AUTHOR INFORMATION

Corresponding Author

*E-mail: rcavicchi@verizon.net. Tel: 301-975-3970.

Present Address

§Center for Devices and Radiological Health, Food and Drug Administration, Silver Spring, Maryland 20993, United States.

Notes

The authors declare no competing financial interest.

ACKNOWLEDGMENTS

We thank Prof. Michael Zachariah for the use of the electro-spray-differential mobility analysis instrument.

REFERENCES

- (1) Loo, C.; Lin, A.; Hirsch, L.; Lee, M. H.; Barton, J.; Halas, N. J.; West, J.; Drezek, R. Nanoshell-Enabled Photonics-Based Imaging and Therapy of Cancer. *Technol. Cancer Res. Treat.* **2004**, *3*, 33–40.
- (2) Huang, X. H.; Jain, P. K.; El-Sayed, I. H.; El-Sayed, M. A. Plasmonic Photothermal Therapy (PpTT) Using Gold Nanoparticles. *Lasers Med. Sci.* **2008**, *23*, 217–228.
- (3) Jain, P. K.; Huang, X. H.; El-Sayed, I. H.; El-Sayed, M. A. Noble Metals on the Nanoscale: Optical and Photothermal Properties and Some Applications in Imaging, Sensing, Biology, and Medicine. *Acc. Chem. Res.* **2008**, *41*, 1578–1586.
- (4) Letfullin, R. R.; Joenathan, C.; George, T. F.; Zharov, V. P. Laser-Induced Explosion of Gold Nanoparticles: Potential Role for Nanophotothermal Therapy of Cancer. *Nanomedicine* **2006**, *1*, 473–480.
- (5) Day, E. S.; Morton, J. G.; West, J. L. Nanoparticles for Thermal Cancer Therapy. *J. Biomech. Eng.* **2009**, *131*, 074001-1–074001-5.
- (6) Zharov, V. P.; Galitovskaya, E. N.; Johnson, C.; Kelly, T. Synergistic Enhancement of Selective Nanophotothermal Therapy with Gold Nanoclusters: Potential for Cancer Therapy. *Lasers Surg. Med.* **2005**, *37*, 219–226.
- (7) Lal, S.; Clare, S. E.; Halas, N. J. Nanoshell-Enabled Photothermal Cancer Therapy: Impending Clinical Impact. *Acc. Chem. Res.* **2008**, *41*, 1842–1851.
- (8) Nam, J.; Won, N.; Jin, H.; Chung, H.; Kim, S. Ph-Induced Aggregation of Gold Nanoparticles for Photothermal Cancer Therapy. *J. Am. Chem. Soc.* **2009**, *131*, 13639–13645.
- (9) Goodrich, G. P.; Bao, L. L.; Gill-Sharp, K.; Sang, K. L.; Wang, J.; Payne, J. D. Photothermal Therapy in a Murine Colon Cancer Model Using near-Infrared Absorbing Gold Nanorods. *J. Biomed. Opt.* **2010**, *15*, 018001-1–018001-8.
- (10) Pissuwan, D.; Valenzuela, S. M.; Miller, C. M.; Cortie, M. B. A Golden Bullet? Selective Targeting of *Toxoplasma Gondii* Tachyzoites Using Anti Body-Functionalized Gold Nanorods. *Nano Lett.* **2007**, *7*, 3808–3812.
- (11) Skirtach, A. G.; Dejugnat, C.; Braun, D.; Susha, A. S.; Rogach, A. L.; Parak, W. J.; Mohwald, H.; Sukhorukov, G. B. The Role of Metal Nanoparticles in Remote Release of Encapsulated Materials. *Nano Lett.* **2005**, *5*, 1371–1377.
- (12) Park, J. H.; von Maltzahn, G.; Ong, L. L.; Centrone, A.; Hatton, T. A.; Ruoslahti, E.; Bhatia, S. N.; Sailor, M. J. Cooperative Nanoparticles for Tumor Detection and Photothermally Triggered Drug Delivery. *Adv. Mater.* **2010**, *22*, 880–885.
- (13) Anderson, L. J. E.; Hansen, E.; Lukianova-Hleb, E. Y.; Hafner, J. H.; Lapotko, D. O. Optically Guided Controlled Release from Liposomes with Tunable Plasmonic Nanobubbles. *J. Controlled Release* **2010**, *144*, 151–158.
- (14) Angelatos, A. S.; Katagiri, K.; Caruso, F. Bioinspired Colloidal Systems Via Layer-by-Layer Assembly. *Soft Matter* **2006**, *2*, 18–23.
- (15) Connor, E. E.; Mwamuka, J.; Gole, A.; Murphy, C. J.; Wyatt, M. D. Gold Nanoparticles Are Taken up by Human Cells but Do Not Cause Acute Cytotoxicity. *Small* **2005**, *1*, 325–327.
- (16) Pittsillides, C. M.; Joe, E. K.; Wei, X. B.; Anderson, R. R.; Lin, C. P. Selective Cell Targeting with Light-Absorbing Microparticles and Nanoparticles. *Biophys. J.* **2003**, *84*, 4023–4032.
- (17) Loo, C.; Lowery, A.; Halas, N. J.; West, J.; Drezek, R. Immunotargeted Nanoshells for Integrated Cancer Imaging and Therapy. *Nano Lett.* **2005**, *5*, 709–711.
- (18) Nehl, C. L.; Grady, N. K.; Goodrich, G. P.; Tam, F.; Halas, N. J.; Hafner, J. H. Scattering Spectra of Single Gold Nanoshells. *Nano Lett.* **2004**, *4*, 2355–2359.
- (19) Hirsch, L. R.; Stafford, R. J.; Bankson, J. A.; Sershen, S. R.; Rivera, B.; Price, R. E.; Hazle, J. D.; Halas, N. J.; West, J. L. Nanoshell-Mediated near-Infrared Thermal Therapy of Tumors under Magnetic Resonance Guidance. *Proc. Natl. Acad. Sci. U. S. A.* **2003**, *100*, 13549–13554.

- (20) Oldenburg, S. J.; Jackson, J. B.; Westcott, S. L.; Halas, N. J. Infrared Extinction Properties of Gold Nanoshells. *Appl. Phys. Lett.* **1999**, *75*, 2897–2899.
- (21) Rasch, M. R.; Sokolov, K. V.; Korgel, B. A. Limitations on the Optical Tunability of Small Diameter Gold Nanoshells. *Langmuir* **2009**, *25*, 11777–11785.
- (22) Cole, J. R.; Mirin, N. A.; Knight, M. W.; Goodrich, G. P.; Halas, N. J. Photothermal Efficiencies of Nanoshells and Nanorods for Clinical Therapeutic Applications. *J. Phys. Chem. C* **2009**, *113*, 12090–12094.
- (23) Knight, M. W.; Halas, N. J. Nanoshells to Nanoeegs to Nanocups: Optical Properties of Reduced Symmetry Core-Shell Nanoparticles Beyond the Quasistatic Limit. *New J. Phys.* **2008**, *10*, 105006-1–105006-11.
- (24) Terentyuk, G. S.; Maslyakova, G. N.; Suleymanova, L. V.; Khlebtsov, N. G.; Khlebtsov, B. N.; Akchurin, G. G.; Maksimova, I. L.; Tuchin, V. V. Laser-Induced Tissue Hyperthermia Mediated by Gold Nanoparticles: Toward Cancer Phototherapy. *J. Biomed. Opt.* **2009**, *14*, 021016-1–021016-9.
- (25) Lee, K. S.; El-Sayed, M. A. Dependence of the Enhanced Optical Scattering Efficiency Relative to That of Absorption for Gold Metal Nanorods on Aspect Ratio, Size, End-Cap Shape, and Medium Refractive Index. *J. Phys. Chem. B* **2005**, *109*, 20331–20338.
- (26) He, G. S.; Zhu, J.; Yong, K. T.; Baev, A.; Cai, H. X.; Hu, R.; Cui, Y. P.; Zhang, X. H.; Prasad, P. N. Scattering and Absorption Cross-Section Spectral Measurements of Gold Nanorods in Water. *J. Phys. Chem. C* **2010**, *114*, 2853–2860.
- (27) Huang, X. H.; Neretina, S.; El-Sayed, M. A. Gold Nanorods: From Synthesis and Properties to Biological and Biomedical Applications. *Adv. Mater.* **2009**, *21*, 4880–4910.
- (28) Zijlstra, P.; Chon, J. W. M.; Gu, M. White Light Scattering Spectroscopy and Electron Microscopy of Laser Induced Melting in Single Gold Nanorods. *Phys. Chem. Phys.* **2009**, *11*, 5915–5921.
- (29) Ratto, F.; Matteini, P.; Rossi, F.; Menabuoni, L.; Tiwari, N.; Kulkarni, S. K.; Pini, R. Photothermal Effects in Connective Tissues Mediated by Laser-Activated Gold Nanorods. *Nanomedicine* **2009**, *5*, 143–151.
- (30) Zuchner, T.; Wackenhut, F.; Failla, A. V.; Meixner, A. J. Nanoscale Characterization of Single Au Nanorods by Confocal Microscopy. *Appl. Surf. Sci.* **2009**, *255*, 5391–5395.
- (31) Tong, L.; Wei, Q. S.; Wei, A.; Cheng, J. X. Gold Nanorods as Contrast Agents for Biological Imaging: Optical Properties, Surface Conjugation and Photothermal Effects. *Photochem. Photobiol.* **2009**, *85*, 21–32.
- (32) Hauck, T. S.; Jennings, T. L.; Yatsenko, T.; Kumaradas, J. C.; Chan, W. C. W. Enhancing the Toxicity of Cancer Chemotherapeutics with Gold Nanorod Hyperthermia. *Adv. Mater.* **2008**, *20*, 3832–3838.
- (33) Huang, Y. F.; Sefah, K.; Bamrungsap, S.; Chang, H. T.; Tan, W. Selective Photothermal Therapy for Mixed Cancer Cells Using Aptamer-Conjugated Nanorods. *Langmuir* **2008**, *24*, 11860–11865.
- (34) Tong, L.; Zhao, Y.; Huff, T. B.; Hansen, M. N.; Wei, A.; Cheng, J. X. Gold Nanorods Mediate Tumor Cell Death by Compromising Membrane Integrity. *Adv. Mater.* **2007**, *19*, 3136–3141.
- (35) Link, S.; Wang, Z. L.; El-Sayed, M. A. How Does a Gold Nanorod Melt? *J. Phys. Chem. B* **2000**, *104*, 7867–7870.
- (36) Lapotko, D.; Lukianova-Hleb, E.; Zhdanok, S.; Rostro, B.; Simonette, R.; Hafner, J.; Konopleva, M.; Andreeff, M.; Conjusteau, A.; Oraevsky, A., Photothermolysis by Laser-Induced Microbubbles Generated around Gold Nanorod Clusters Selectively Formed in Leukemia Cells - Art. No. 68560k. In *Photons Plus Ultrasound: Imaging and Sensing 2008: The Ninth Conference on Biomedical Thermoacoustics, Optoacoustics, and Acoustic-Optics*; Oraevsky, A. A., Wang, L. V., Eds.; SPIE: Bellingham, WA, 2008; Vol. 6856, pp K8560–K8560.
- (37) Hu, M.; Petrova, H.; Chen, J. Y.; McLellan, J. M.; Siekkinen, A. R.; Marquez, M.; Li, X. D.; Xia, Y. N.; Hartland, G. V. Ultrafast Laser Studies of the Photothermal Properties of Gold Nanocages. *J. Phys. Chem. B* **2006**, *110*, 1520–1524.
- (38) Hasan, W.; Stender, C. L.; Lee, M. H.; Nehl, C. L.; Lee, J.; Odum, T. W. Tailoring the Structure of Nanopyramids for Optimal Heat Generation. *Nano Lett.* **2009**, *9*, 1555–1558.
- (39) Huang, X. H.; El-Sayed, I. H.; Qian, W.; El-Sayed, M. A. Cancer Cell Imaging and Photothermal Therapy in the near-Infrared Region by Using Gold Nanorods. *J. Am. Chem. Soc.* **2006**, *128*, 2115–2120.
- (40) Koblinski, P.; Cahill, D. G.; Bodapati, A.; Sullivan, C. R.; Taton, T. A. Limits of Localized Heating by Electromagnetically Excited Nanoparticles. *J. Appl. Phys.* **2006**, *100*.
- (41) Avedisian, C. T.; Cavicchi, R. E.; McEuen, P. L.; Zhou, X. J., Nanoparticles for Cancer Treatment Role of Heat Transfer. In *Interdisciplinary Transport Phenomena: Fluid, Thermal, Biological, Materials, and Space Sciences*; Sadhal, S. S., Ed.; New York Academy of Sciences: New York, 2009; Vol. 1161, pp 62–73.
- (42) Sassaroli, E.; Li, K. C. P.; O'Neill, B. E. Numerical Investigation of Heating of a Gold Nanoparticle and the Surrounding Microenvironment by Nanosecond Laser Pulses for Nanomedicine Applications. *Phys. Med. Biol.* **2009**, *54*, 5541–5560.
- (43) Richardson, H. H.; Carlson, M. T.; Tandler, P. J.; Hernandez, P.; Govorov, A. O. Experimental and Theoretical Studies of Light-to-Heat Conversion and Collective Heating Effects in Metal Nanoparticle Solutions. *Nano Lett.* **2009**, *9*, 1139–1146.
- (44) Link, S.; El-Sayed, M. A. Shape and Size Dependence of Radiative, Non-Radiative and Photothermal Properties of Gold Nanocrystals. *Int. Rev. Phys. Chem.* **2000**, *19*, 409–453.
- (45) Hu, M.; Hartland, G. V. Heat Dissipation for Au Particles in Aqueous Solution: Relaxation Time Versus Size. *J. Phys. Chem. B* **2002**, *106*, 7029–7033.
- (46) Hartland, G. V.; Hu, M., Photophysics of Metal Nanoparticles: Heat Dissipation and Coherent Excitation of Phonon Modes. In *Physical Chemistry of Interfaces and Nanomaterials*; Zhang, J. Z., Wang, Z. L., Eds.; SPIE: Bellingham, WA, 2002; Vol. 4807, pp 166–176.
- (47) Zharov, V. P.; Letfullin, R. R.; Galitovskaya, E. N. Microbubbles-Overlapping Mode for Laser Killing of Cancer Cells with Absorbing Nanoparticle Clusters. *J. Phys. D: Appl. Phys.* **2005**, *38*, 2571–2581.
- (48) Lapotko, D.; Lukianova, E.; Potapnev, M.; Aleinikova, O.; Oraevsky, A. Method of Laser Activated Nano-Thermolysis for Elimination of Tumor Cells. *Cancer Lett.* **2006**, *239*, 36–45.
- (49) Hleb, E. Y.; Hafner, J. H.; Myers, J. N.; Hanna, E. Y.; Rostro, B. C.; Zhdanok, S. A.; Lapotko, D. O. Lantcet: Elimination of Solid Tumor Cells with Photothermal Bubbles Generated around Clusters of Gold Nanoparticles. *Nanomedicine* **2008**, *3*, 647–667.
- (50) Hleb, E. Y.; Hu, Y.; Drezek, R. A.; Hafner, J. H.; Lapotko, D. O. Photothermal Bubbles as Optical Scattering Probes for Imaging Living Cells. *Nanomedicine* **2008**, *3*, 797–812.
- (51) Takahashi, H.; Niidome, T.; Nariai, A.; Niidome, Y.; Yamada, S. Gold Nanorod-Sensitized Cell Death: Microscopic Observation of Single Living Cells Irradiated by Pulsed near-Infrared Laser Light in the Presence of Gold Nanorods. *Chem. Lett.* **2006**, *35*, 500–501.
- (52) Huang, X. H.; Kang, B.; Qian, W.; Mackey, M. A.; Chen, P. C.; Oyelere, A. K.; El-Sayed, I. H.; El-Sayed, M. A. Comparative Study of Photothermolysis of Cancer Cells with Nuclear-Targeted or Cytoplasm-Targeted Gold Nanospheres: Continuous Wave or Pulsed Lasers. *J. Biomed. Opt.* **2010**, *15*.
- (53) Takami, A.; Yamada, H.; Nakano, K.; Koda, S. Size Reduction of Silver Particles in Aqueous Solution by Laser Irradiation. *Jpn. J. Appl. Phys., Part 2* **1996**, *35*, L781–L783.
- (54) Takami, A.; Kurita, H.; Koda, S. Laser-Induced Size Reduction of Noble Metal Particles. *J. Phys. Chem. B* **1999**, *103*, 1226–1232.
- (55) Kamat, P. V.; Flumiani, M.; Hartland, G. V. Picosecond Dynamics of Silver Nanoclusters. Photoejection of Electrons and Fragmentation. *J. Phys. Chem. B* **1998**, *102*, 3123–3128.
- (56) Link, S.; Burda, C.; Nikoobakht, B.; El-Sayed, M. A. Laser-Induced Shape Changes of Colloidal Gold Nanorods Using Femto-second and Nanosecond Laser Pulses. *J. Phys. Chem. B* **2000**, *104*, 6152–6163.
- (57) Giammanco, F.; Giorgetti, E.; Marsili, P.; Giusti, A. Experimental and Theoretical Analysis of Photofragmentation of Au Nanoparticles by Picosecond Laser Radiation. *J. Phys. Chem. C* **2010**, *114*, 3354–3363.
- (58) Matsuo, N.; Muto, H.; Miyajima, K.; Mafune, F. Single Laser Pulse Induced Aggregation of Gold Nanoparticles. *Phys. Chem. Chem. Phys.* **2007**, *9*, 6027–6031.

(59) Muto, H.; Miyajima, K.; Mafune, F. Mechanism of Laser-Induced Size Reduction of Gold Nanoparticles as Studied by Single and Double Laser Pulse Excitation. *J. Phys. Chem. C* **2008**, *112*, 5810–5815.

(60) Yamada, K.; Tokumoto, Y.; Nagata, T.; Mafune, F. Mechanism of Laser-Induced Size-Reduction of Gold Nanoparticles as Studied by Nanosecond Transient Absorption Spectroscopy. *J. Phys. Chem. B* **2006**, *110*, 11751–11756.

(61) Hleb, E. Y.; Lapotko, D. O. Photothermal Properties of Gold Nanoparticles under Exposure to High Optical Energies. *Nanotechnology* **2008**, *19*, 355702-1–355702-10.

(62) Lapotko, D. Optical Excitation and Detection of Vapor Bubbles around Plasmonic Nanoparticles. *Opt. Express* **2009**, *17*, 2538–2556.

(63) Heath, J. R.; Davis, M. E. Nanotechnology and Cancer. *Annu. Rev. Med.* **2008**, *59*, 251–265.

(64) Certain commercial instruments are identified to adequately specify the experimental procedure. In no case does such identification imply endorsement by the National Institute of Standards and Technology.

(65) Mulholland, G. W.; Donnelly, M. K.; Hagwood, C. R.; Kukuck, S. R.; Hackley, V. A.; Pui, D. Y. H. Measurement of 100 Nm and 60 Nm Particle Standards by Differential Mobility Analysis. *J. Res. Natl. Inst. Stand. Technol.* **2006**, *111*, 257–312.

(66) Kaszuba, M.; Connah, M. T.; McNeil-Watson, F. K.; Nobbmann, U. Resolving Concentrated Particle Size Mixtures Using Dynamic Light Scattering. *Part. Part. Syst. Charact.* **2007**, *24*, 159–162.

(67) Berne, B. J.; Pecora, R. *Dynamic Light Scattering: With Applications to Chemistry, Biology, and Physics*; Wiley: New York, 1976; p. 376.

(68) Tsai, D. H.; Zangmeister, R. A.; Pease, L. F.; Tarlov, M. J.; Zachariah, M. R. Gas-Phase Ion-Mobility Characterization of Sam-Functionalized Au Nanoparticles. *Langmuir* **2008**, *24*, 8483–8490.

(69) Guha, S.; Pease, L. F.; Brorson, K. A.; Tarlov, M. J.; Zachariah, M. R. Evaluation of Electrospray Differential Mobility Analysis for Virus Particle Analysis: Potential Applications for Biomanufacturing. *J. Virol. Methods* **2011**, *178*, 201–208.

(70) Li, M. D.; Guha, S.; Zangmeister, R.; Tarlov, M. J.; Zachariah, M. R. Quantification and Compensation of Nonspecific Analyte Aggregation in Electrospray Sampling. *Aerosol Sci. Technol.* **2011**, *45*, 849–860.

(71) Finsy, R. Particle Sizing by Quasi-Elastic Light-Scattering. *Adv. Colloid Interface Sci.* **1994**, *52*, 79–143.

(72) Torrisi, L.; Picciotto, A.; Ando, L.; Gammino, S.; Margarone, D.; Laska, L.; Pfeifer, M.; Krasa, J. Pulsed Laser Ablation of Gold at 1064 Nm and 532 Nm. *Czech. J. Phys.* **2004**, *54*, 421–430.

(73) Link, S.; El-Sayed, M. A. Size and Temperature Dependence of the Plasmon Absorption of Colloidal Gold Nanoparticles. *J. Phys. Chem. B* **1999**, *103*, 4212–4217.

(74) Dubin, S. B.; Clark, N. A.; Benedek, G. B. Measurement of Rotational Diffusion Coefficient of Lysozyme by Depolarized Light Scattering - Configuration of Lysozyme in Solution. *J. Chem. Phys.* **1971**, *54*, 5158–5164.

(75) Orendorff, C. J.; Sau, T. K.; Murphy, C. J. Shape-Dependent Plasmon-Resonant Gold Nanoparticles. *Small* **2006**, *2*, 636–639.

(76) Murphy, C. J.; Thompson, L. B.; Chernak, D. J.; Yang, J. A.; Sivapalan, S. T.; Boulos, S. P.; Huang, J. Y.; Alkilany, A. M.; Sisco, P. N. Gold Nanorod Crystal Growth: From Seed-Mediated Synthesis to Nanoscale Sculpting. *Curr. Opin. Colloid Interface Sci.* **2011**, *16*, 128–134.